Combined Convolutional Neural Network for High Frequency Restoration in Acoustic Impedance Images

Isaac Sacramento
Department of Informatic and Statistics
Federal University of Santa Catarina
Florianpolis, Brazil
isaac.sacramento@posgrad.ufsc.br

Mauro Roisenberg
Department of Informatic and Statistics
Federal University of Santa Catarina
Florianpolis, Brazil
mauro.roisenberg@ufsc.br

Rodrigo Exterkoetter
Department of Informatic and Statistics
Federal University of Santa Catarina
Florianpolis, Brazil
rodrigoext@gmail.com

Leando P. de Figueiredo
Department of Physics
Federal University of Santa Catarina
Florianpolis, Brazil
leandrop.fgr@gmail.com

Bruno Rodrigues
Petrobras Research Center
Petrobras
Rio de Janeiro, Brazil
bbrodrigues@gmail.com

Abstract—Domain-specific methods for deblurring particular sorts of objects have gained increasing attention due to the ineffectiveness of generic methods. We present a simple and effective convolutional neural network that deblurs synthetic acoustic impedance images. The architecture of our model is divided into two basic structures: convolutional layers and regression unit. The convolutional layers highlight edges and contours related to interfaces between rock layers whereas the regression layer performs a non-linear estimation of acoustic impedance values. We consider a training dataset composed by wedge shaped images, positioned at four different angles. In our work, we adopt a strong supervised learning that exploit the dataset of artificially blurred and high resolution images. We also present an analysis comparing the frequency band-width among the latent, blurry, and deblurred images. We additionally address the requirement of deep learning for the huge amount of training examples by inserting rectified linear units (ReLU) and keeping the network architecture simple. Experimental results on synthetic test images demonstrate the efficacy of the proposed method.

Index Terms—convolutional neural network, acoustic impedance, deblurring, seismic inversion, frequency recovering

I. INTRODUCTION

Deblurring is the task of estimating a sharp latent image, given a blurry image as input. According to [1], it is not observable in the literature an algorithm for deblurring all objects, i.e., domain-specific knowledge should, somehow, be incorporated to the algorithm in order to proceed effective deblurring. In the oil exploration field, the seismic data acquisition and its inversion to acoustic impedance attribute typically generates blurry images of the subsurface in such a way that it does not clearly observe the interfaces between

different rock layers nor the geological structures that make up the reservoir, such as channels, fans, traps, faults, connectivity patterns, etc. Obtaining high resolution acoustic impedance images, through seismic inversion methods, is a critical part in oil reservoir characterization. Despite the notorious efficiency of inversion methods, post-inversion images deblurring has not received much attention.

Reservoir characterization aims to determine the multidimensional structure and properties of an oil field. To achieve this goal, it is essential to combine, through an inversion algorithm, the information, knowledge and available data about the field, in such a way that it is possible to make the quantitative predictions about the reservoir behavior [2]. Using the seismic data in deep-water reservoir modeling leads to errors in estimating the reservoir properties because such data do not allow the wider understanding of the field under study [35]. To succeed in seismic inversion, it is necessary to include strategies to deal with multiple sources of uncertainties. Specifically, the limited band-width of the seismic data leads to a misinterpretation of the resulting acoustic impedance models. According to [3], improving the resolution of seismic inversion is possible by adding high frequency in the acquisition and processing seismic data. However, the earth attenuation, high-frequency noise and other sources cause the lack of high and low frequencies in seismic data. Thus, deblurring the acoustic impedance models, as a post-inversion refinement process, should lead to a more accurate interpretation of the impedance models.

We approach the acoustic impedance deblurring through a Convolutional Neural Network (CNN) model. CNN is a framework of deep learning which has been used in a wide sort of machine learning tasks. The availability of benchmarks [4] and the advances in Graphical Processing Unit (GPU) [5]

allowed CNN to outperform state-of-the-art techniques in detection [6], [7], model-free tracking [8], and classification [9]. With excellence in feature learning, CNN achieved notorious success in image and video classification [10], [11], action and speech recognition [12], [13]. Under the perspective of the reservoir characterization, CNN has been applied to lithofacies recognition [14] and calculation [15]. However, there is a lack of researches on improving the resolution of images resulting from inversion processes.

In this paper, we propose a new multilayer convolutional network model to perform deblurring in post-inversion acoustic impedance. Each network layer maps higher level features originating in the previews layers through convolutional blur kernels. To perform this mapping, the kernels (also named weights) are adjusted by minimizing a loss function. The model enhances the resolution of acoustic impedance images, resulting in sharp images with increased high-frequency bandwidth and lower noise. In order to train the model, we blur a set of the synthetic acoustic impedance images to create a dictionary of images of high and low resolution. Then, the pairs of blur and latent images are normalized and presented to the network as input and target, respectively. In our approach, the domain-specific knowledge used in deblurring acoustic impedance impedance images is commonly obtained through training images containing geological knowladge. Generally, the images are obtained from a specialist's (geologist or geophysicist) knowledge about relevant characteristics of the reservoir for which one wishes enhancing the impedance images. The core concept of our architecture is the combination of the convolutional layers with regression layers, thus the convolutional layers learn the spatial structures existing in different acoustic impedance images, while the regression layer proceed the prediction of the property values.

II. Theoretical Foundations and Related Works

Inversion theory is used in several areas to infer parameters values related to physical processes based on experimental data. Inversion modeling refers to using the current measurements of observable physical parameters in order to infer the current model parameters (not observable). The inversion problem is described as (1)

$$m = F^{-1}(d) \qquad (1)$$

where, F is the investigated physical system, and relates a set of model parameters $m = (m_1, m_2, ..., m_n) \subset R^n$ estimated through the observed data $d \in R^s$. Geophysical methods frequently involve the solution and assessment of inversion problems. Studying these issues allow inferring physical properties distributions in the earth subsurface, using measured data. Among these data, the seismic data are mainly used in seismic inversion, which plays an important role in reservoir characterization. From a practical perspective, solving seismic inversion problems improves the exploration and management in oil industry, once the seismic data are highly correlated to petrophysical properties, e.g., density and porosity in subsurface.

The offshore seismic data are the main observable data used in seismic inversion. To perform seismic acquisition, one sends pulses through a controlled artificial source and captures the vertical component responses in function of time. The seismic data are a composition of the wave pulse used in the acquisition (named wavelet) and the characteristic of the interfaces between rock layers, on which the wavelet reflects. This rock layer characteristic is called a reflectivity coefficient and it is calculated as (2)

$$r(t) = \frac{z(t + \delta t) - z(t)}{z(t + \delta t) + z(t)}, \qquad (2)$$

where, $z(t)$ is the acoustic impedance, in function of time t, defined as $z(t) = \rho(t)v(t)$, where $\rho(t)$ is the rock density and $v(t)$ the propagation velocity of acoustic wave. Therefore, the seismic data $d(t)$ is modeled as a discrete convolution operation $*$ of the wavelet s with the reflectivity coefficient r as (3)

$$d(t) = s(\tau) * \sum_{j-1}^{N} r(t - t_j)\delta(t - t_j) + e_d(t) \qquad (3)$$

where, N is the number of subsurface layers, $e_d(t)$ is a random noise in function of time. One ideal wavelet is a delta pulse with complete frequency band-width, however, in practice wavelets have their band-width generally limited from $6Hz$ to $65Hz$. By consequence, the images resulting from the seismic inversion will keep their frequency spectrum limited. According to [16], a good acoustic impedance model contains more information than the seismic data, because the inversion process contains additional information originated from well-logs, for exemple, a low-frequency model. The well-logs are real data measured in wells spread along the field. With the local acoustic impedance it is possible to calculate the low-frequency model by interpolation between wells [17], [18]. Despite of the low-frequency model, the final model for acoustic impedance still lacks of high resolution details.

Deblurring is generally modeled as the convolution of a blur kernel k with a latent image I:

$$y = k \otimes I + n \qquad (4)$$

where n is the noise. Since k, I and n are unknown, the problem is highly ill-posed and admits infinite solutions for k and I. Within this context, blind deconvolution refers to the inference of the sharp image I, given only the blurry image y, without any knowledge regarding the kernel k and the noise n [20].However, if k is assumed to be known, the deblurring is called non-blind deconvolution [19]. Several works have developed different deblurring methods for specific purposes. Blind deconvolution methods are widely investigated in image processing [21]. For the last six years, considerable effort has been made in single image [22]–[25] and multi-image [26], [27] blind deconvolutions. Applying blind deconvolution generally implies in making assumptions on blur kernels and/or on latent images. For example, assuming sparsity of blur kernel or that natural images have super-Gaussian statistics. The second assumption leads to the use

of image priors on inference process and, consequently, to the maximum *a posteriori* (MAP) estimation [22]. However, [28] show that deblurring methods based on this prior tend to favor blurry images over original latent images.

The Bayesian inference approach [28] outperforms the MAP based methods. It marginalizes the image from the optimization step, while estimating the unknown blur. The authors show that it is possible to define a class of prior image based on natural image statistics, suitable enough to represent sharp images features. This prior formulation makes possible to use Bayesian inference in the estimation of the unknown image and the blur kernel. According to [29], defining a gradient prior, by itself, is not sufficient to reach a sharp image, instead, they search in a dataset for a prior that densely correspond to the blurry image similar to a sharp image. This search is an interactively optimization over the correspondence between the images, the kernel and the sharp image estimation. Even though [30] suggest a generalization for the method proposed by [29], it still requires a similar reference image, which is not always available.

The optimization methods previously described use a set of priors based on generic image statistics or domain-specific priors. It has been demonstrated that these methods work properly on synthetic blurs. However, new studies show that they fail when applied to real world blurry images [31] and take a severe computational cost [32]. In contrast, the learning-based methods have gained attention with the resumption and recent advances in convolutional neural networks (CNN). The adequate hyper-parameter adjustment allows CNN to learn non-linear function or blur kernels. Thus, deblurring becomes a function of a blurry image I and a set of parameters p as (5)

$$y = \sigma(I, p) \tag{5}$$

Learning-based methods focus on developing a model to learn the function σ [33] and to perform non-blind deblurring [32]. [34] teaches a CNN to recognize motion kernels and performs non-blind deconvolution in dense motion field estimate, in addition, [33] minimize regularized l_2 in order to perform text deblurring.

III. Data and Methods

A. Generating the Training Dataset

The experiments described in this paper perform on a set of synthetic acoustic impedance images. Using synthetic models to test and parameterize algorithms is a common practice in reservoir characterization [35]. It allows studying the results of the algorithms without external interference and performing efficient interpretations and assessments. According to [36], wedge shaped models is a straight way to analysis the seismic model and inversion processes. It reproduces reservoir contexts such as stratigraphic refinements, edges and channel structures in a realistic manner.

The training set generation occurs in two steps. The fist step creates a set of wedge shapes represented by images with size 32 x 32. The wedge shapes represent the reservoir and they
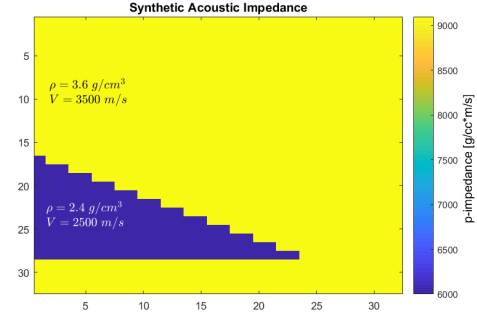

Fig. 1. Acoustic impedance model generation. Wedge with reference values for density and compression velocity.
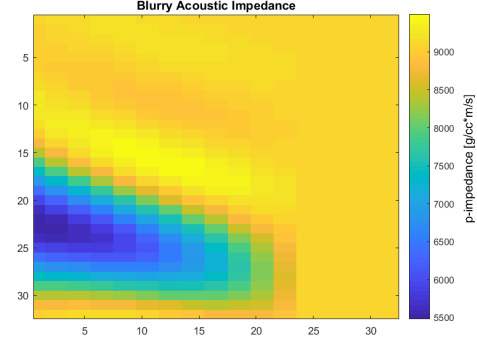

Fig. 2. Acoustic impedance blurred model.

randomly vary in width and length. The second step fills the lithology with values of petrophysical properties. In order to simplify the assessments and conclusions, we fill the lithology structures with constant reference values of rock densities and compression velocity observed in the literature [37]. The acoustic impedance is calculated using the density and velocity models and the images in high resolution model are obtained, as illustrated in Fig. 1.

In a real scenario, the blurry acoustic impedance is the result of an acoustic inversion method, such as Maximum *a posteriori* [17], [18], Sparse Spike [38] and Recursive Inversion [39], using seismic data with limited band-with. However, for experimental purpose, the acoustic impedance models were filtered and the high frequencies were removed to obtain the blurry images, as illustrated in Fig. 2. This way, the supervised learning is performed with the high resolution images and blurred images. To increase the number of examples in the training dataset we rotate the impedance models to establish the wedge structure in four different angles (0°, 90°, 180° and 270°). This approach allows the model learning an wide edge variability in wedges images.

B. Proposed Architecture

The workflow of the proposed method consists of the following steps:

- Generate the synthetic impedance images;
- Blur the images through a low-pass filter;
- Train the convolutional model with the pair of high and low resolution images;
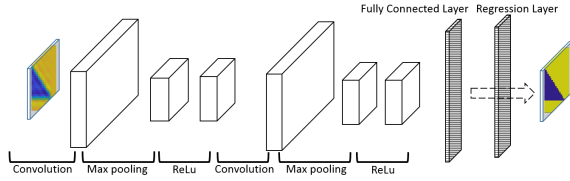
Fig. 3. Proposed model architecture.

- Test the model with different blurry images;
- Assess the result for the testing output.

The CNN is a well established method for pattern recognition and image classification. Thus, an important breakthrough when applying CNN to deal with physical property images is developing a model capable of solving regression tasks. The model presented in this paper is able to solve two important problems related to deblurring images of physical properties : (1) learning the spacial patterns in the low resolution training images and (2) predicting each pixel intensity value in the new higher resolution image. To reach these two goals, our model, outlined in Fig. 3, comprises f two major components that are combined to perform deblurring and physical property prediction jointly: (1) convolutional component and (2) regression component. The convolutional component is a two layer structure that maps a blurry image to a non-blurred model, while the regression layer is supposed to predict the continuous values of each pixel representing the acoustic impedance value. The state-of-the-art CNN models for image deblurring [1] and super-resolution [40] classify each pixel in the input image. Using these methods to solve the issue of deblurring continuous physical properties implies a discretization of each pixel in order to generate an image file. However, returning to the original data, results in information loss what represents a serious inconvenient. Thus, combining the convolutional approach with the regression layer to deblur and predict the physics property represents a relevant advance.

C. Implementation Details

The model is implemented using the Deep Learning toolbox delivered in MATLAB R2017A. Our model is comprised of a simple architecture with two convolutional layers. Each one of them is configured with 50 kernels, sized 5 x 5 and stride 1, meaning that after each convolution operation the blur kernel is shifted one position in each direction. After each convolutional layer we will proceed a maximum pooling operation to obtain the maximum value of small regions in the input image and obtain statistical summaries of these regions. We will also apply rectified linear units (ReLU) after each pooling layer in order to speed up the training step and to learn sensible features from the images, following the proposal of [41]. After the second regularization layer, we add a fully connected layer, which maps the convolution layer's output to 1024 neurons. Finally, the output layer will be comprised of a regression unit to predict the intensity of acoustic impedance in each pixel. The output vector is then resized to the original image dimension.

For training the network, we will use a mini-batch with size of 32 training examples and we will adopt an exponentially decreasing learning rate (initially set to 0.005), decreasing every iteration in a total of 100 iterations. It should be noted that, once the wedge shapes are randomly generated, every image is different and each one is introduced only once to the network, this way avoiding over-fitting. The network weights will initialize randomly and the model will perform a supervised learning through a dictionary containing pairs of low resolution and high resolution images. The Stochastic Gradient Descent with Momentum (SGDM) [42] adjusts the network weights in every layer by minimizing the Mean Squared Error (MSE) in each batch of images. Thus, after the training phase, the model will be capable of deblurring any other wedge shaped acoustic impedance image not presented in the training dataset. The output image recovers the high frequencies and will show higher similarity to the high resolution image than to the blurred image, according to established metric. The model will be adjusted to deblur a wide variety of wedge shapes and impedance values. Thus, the images whose wedges the model are unable to predict, will be used to form a new training dataset and the model can then be retrained. Three metrics will assess the performance of our convolution network: Fast Fourier Transform Index - FFTI (6), Rooted Mean Square Error - RMSE (7). The FFTI is a similarity metric calculated based on the fast fourier transform (FFT) of each image. It is introduced by [43] and calculates as

$$C = \frac{(\sum_{i=1}^{N} F_{1i}F_{2i} - N\bar{F}_1\bar{F}_2)^2}{(\sum_{i=1}^{N} |F_{1i}|^2 - N\bar{F}_1^2)(\sum_{i=1}^{N} |F_{2i}|^2 - N\bar{F}_2^2)}, \quad (6)$$

where, for each frequency, an intensity value is calculated from the real and complex parts of the fourier transform. F_{1i} represents the intensity value of i-th *pixel* in the first image and F_{2i} is the intensity value of i-th *pixel* in the second image. $\bar{F}_1$ e $\bar{F}_2$ are the mean frequencies in each image. The closer FFTI is to 1, the higher the similarity between images. Additionally, we will use the frequency spectrum to show the graphics of magnitudes, which allow distinguishing what high frequencies are added to the acoustic impedance after the low resolution images pass through the trained CNN.

$$RMSE = \sqrt{\frac{(\sum_{i=1}^{N} (x_i - y_i)^2)}{N}}, \quad (7)$$

IV. EXPERIMENTS AND RESULTS

To build the training dataset we generate 500 images of random wedges. Due to the predefined hyperbolic tangent sigmoid ($tansig$) transfer function in the regression unit, we normalize the acoustic impedance to values between 0 and 1, and the results are presented in terms of this normalization. The normalized images are then rotated according to the established angles mentioned in Section III, then comprising a total of 2000 images. By doing so, we present to the network the same lithologies in different positions and expect the network to identify general sorts of wedges, in different angles. The rotated images are blurred by applying a low-pass filter
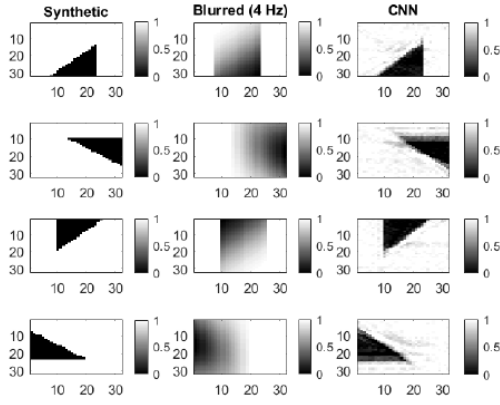
Fig. 4. First test case: the wedges are positioned in $0°$, $90°$, $180°$ and $270°$ and the acoustic impedance values are normalized to 0 and 1.

Fig. 5. The wedges are positioned in $0°$, $90°$, $180°$ and $270°$. The acoustic impedance values are normalized to 0.3 and 0.7.

TABLE I
TABLE OF METRIC VALUES FOR WEDGES WITH ACOUSTIC IMPEDANCE
NORMALIZED TO 0 AND 1.

Metrics	Blurry Image (MSE - FFTI)	CNN (MSE - FFTI)
Example 1	0.1990 — 0.9548	0.1195 — 0.9884
Example 2	0.3132 — 0.8854	0.1639 — 0.9682
Example 3	0.1990 — 0.9548	0.1194 — 0.9838
Example 4	0.3132 — 0.8970	0.1736 — 0.9627

TABLE II
TABLE OF METRIC VALUES FOR WEDGES WITH ACOUSTIC IMPEDANCE
NORMALIZED TO 0.3 AND 0.7.

	Blurry Image (MSE - FFTI)	CNN (MSE - FFTI)
Example 1	0.0876 — 0.9463	0.0593 — 0.9694
Example 2	0.1135 — 0.9093	0.0721 — 0.9693
Example 3	0.0876 — 0.9463	0.0549 — 0.9734
Example 4	0.1135 — 0.9101	0.0699 — 0.9730

with $4Hz$ cutting frequency, then the pairs of blurred and not-blurred images are used to adjust the model weights.

In the following subsections we present the results divided into four cases. First, we tested the wedges rotated according to the established angles and with acoustic impedance values normalized to 0 and 1. Next, we tested images with impedance values normalized to the interval between 0.3 and 0.7, thereby removing images out of the range used during the training phase. We then assess the model response to images blurred with different cutting frequencies. Finally, we presented to the model wedges with random shapes, rotated at random angles.

A. Integer Angles Rotated Wedges

We first tested the network capability to correctly model the shape of wedges and to deblur their edges and contours in a simple perspective. The training and testing images had the same reference values for density and compression velocity. They differed from each other only by the shape. Comparing the blurry images (middle column in Fig. 4) and the CNN outputs (right column in Fig. 4), the CNN outputs notably achieved sharper images and accurately predicted the pixel intensities. Tab. I shows that the error values related to the network output and the latent images are considerably lower than the RMSE related to the latent and the blurry images. Furthermore, the FFTI increased and indicates more similarity among the outputs and the latent images, except for the first image in which the FFTI shows non-representative changes.

In the following scenario, we arbitrarily change the normalized impedance in both lithologies to values 0.7 out of the wedges and 0.3 into them. These values are different from
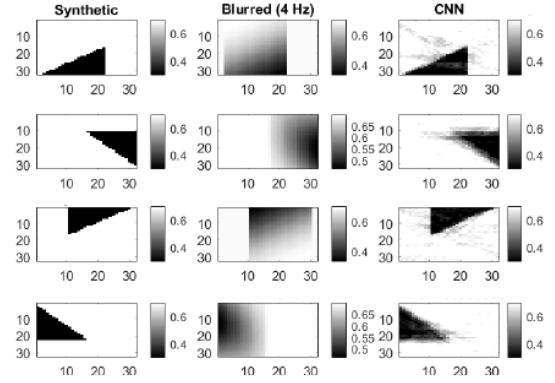
those learned by the model during the training phase and we tested the model generalization capability. Once the model was trained to pixels in the range 0 and 1, the model poorly extrapolated to the new values. Thus, we retrained the model with a new dataset containing 30% of images normalized to the mentioned impedance values (0.7, 0.3) and tested it with the blurry images shown in Fig. 5. It is noticeable that the network trained with the new dataset, learned the wedge shapes and the new pixel intensities, with low variance. Considering the CNN outputs, the metric values in Tab. II show that the RMSE decreased, while the similarity with the latent image increased.

In a real data scenario, signal attenuation caused by the depth would lead to different blurring profiles in post-inversion images. In order to investigate this scenario, we blur each synthetic image with a different cutting frequency, randomly choosing between 1 and $20Hz$. Figure 6 shows that the model deblurred images containing different blurry resolution, and highlighted edges as well as possible interfaces between rock layers. As illustrated in Fig. 6, the experiments revealed that the model trained with images blurred in $4Hz$ correctly deblurred images in the range of higher attenuation. However, the model was unable to properly deblur images with higher frequencies. Metrics in Tab. III show that the RMSE of each CNN output is lower than the RMSE of the blurry images, except for the image blurred with $15Hz$ cutting frequency.

B. Randomly Shapes and Random Positions

Hier, we tested the network capability to deblur wedges with random shapes, at random position in the image. Additionally, this test case is comprised of images with acoustic impedance normalized to values equal to 0 and 1, moreover
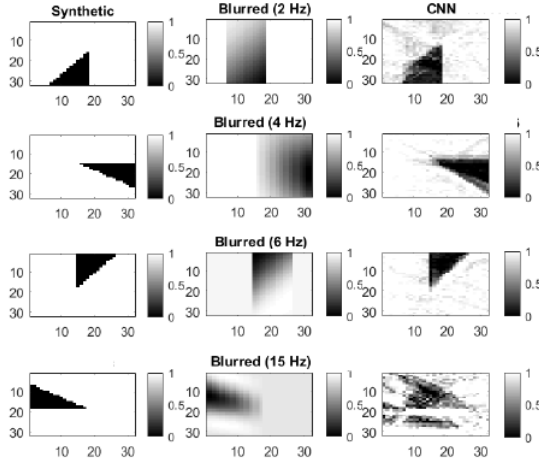
Fig. 6. The wedges are positioned in 0°, 90°, 180° and 270°. The acoustic impedance models are blurred using different cutting frequencies.

Fig. 7. Examples in which the wedges have random shapes and are positioned at random angles.

TABLE III
TABLE OF METRIC VALUES FOR WEDGES BLURRED WITH DIFFERENT
CUTTING FREQUENCIES.

	Blurry Image (MSE - FFTI)	CNN (MSE - FFTI)
Example $(2Hz)$	0.2074 — 0.9533	0.1981 — 0.9660
Example $(4Hz)$	0.3136 — 0.8927	0.1770 — 0.9710
Example $(6Hz)$	0.1539 — 0.9756	0.1385 — 0.9898
Example $(15Hz)$	0.1904 — 0.9676	0.5561 — 0.8053

TABLE IV
TABLE OF METRIC VALUES FOR WEDGES IN RANDOM POSITIONS AND
ACOUSTIC IMPEDANCE NORMALIZED TO 0 AND 1.

	Blurry Image (MSE - FFTI)	CNN (MSE - FFTI)
Example 1	0.2310 — 0.9241	0.2170 — 0.9146
Example 2	0.2180 — 0.9441	0.2155 — 0.9280
Example 3	0.2196 — 0.9464	0.1957 — 0.9447
Example 4	0.2234 — 0.9562	0.2031 — 0.9603

images blurred at $20Hz$ were added to the training dataset. It is observable in Fig. 7 that the model presented higher uncertainty in modeling the edges and corners. On the other side, due to the same range of values in the training and testing images, the model kept its predictive capacity. This result is evident in the metrics' values (Tab. IV). The model's outputs presented RMSE values lower than the blurry images. However, according to the FFTI, only in example 4 the model's output showed higher similarity to the latent image. That is explained by the higher uncertainty related to the wedge shapes. A mitigation for this problem is adding examples of this image, in different blurry frequencies, to the network training dataset, as stated previously in Section IV-A.

C. Frequency Recovering

A relevant aspect of deblurring acoustic impedance images is the evidence of high frequencies recovering in the deblurry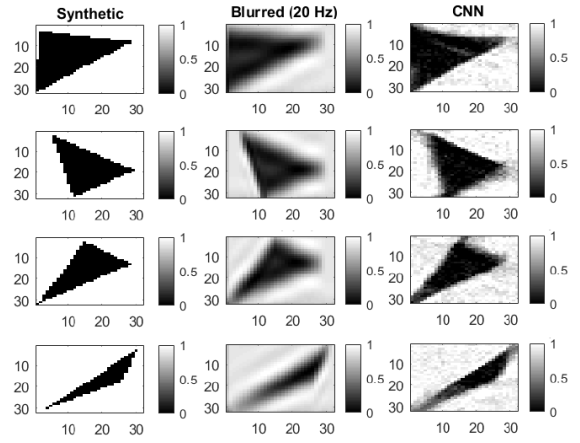 images and in the resulting seismic data. Here, we used the Fourier transform to introduce the graphs containing frequency magnitudes of each image in our test examples.

The frequency magnitudes in our first test case, illustrated in Fig. 8a, show that the model precisely recovered the frequency spectrum of the original image. The resulting acoustic impedance shows increasing frequency magnitude in the range between $20Hz$ and $50Hz$, and between $60Hz$ and $100Hz$. This test case represents the ideal result due to the decreasing error, increasing similarity, and frequency band-with in the CNN output images. Next, by training the model with a new dataset containing acoustic impedance images normalized to 0.3 and 0.7, we recovered the frequency magnitudes slightly lower than the ones of latent images, in the range of middle frequencies (Fig. 8b). It is noticeable that the model deblurred with more low frequency than exist in latent images. This result reflects the insertion of only 30% images normalized to the mentioned range of values. Figure 8c shows the frequency spectrum recovering for images blurred with random cutting frequencies. Clearly, our model is able to deblur and highlight interfaces separating rock layers for impedance images containing different blurs caused by attenuation elements in seismic data acquisition. However, it shows increasing uncertainty and degradation as long as the difference among the blurry image frequencies and the ones learned by the model increases. Finally, for the test images with random shape and position, the proposed model recovered magnitudes slightly lower than in the latent images (Fig. 8d). These results still depend on a new assessment due to the increase in frequency magnitudes between $10Hz$ and $60Hz$, whereas the metrics suggest lower error and lower similarity when comparing the model outputs and the blurry images.

V. CONCLUSION

In summary, we introduced a convolutional neural network model for recovering high-quality synthetic acoustic impedance images from degraded ones (blurry, noisy). Moreover, we introduced a simple architecture composed of two components: convolutional and regression. We demonstrated

that the proposed CNN recovers the high frequencies magnitudes absent in blurry images. Experimental results validate the proposed method in different blurry scenarios. The methodology is promising for deblurrying acoustic impedance images due to its capability to learn blurry kernerls, highlight edges and contour in wedge shaped lithologies in addition to predict the continuousness of rock property. For future work, we will aim to assess the model on real post-inversion acoustic impedance images and investigate its influence on seismic profiles.

REFERENCES

[1] G. G. Chrysos, and S. Zafeiriou, "Deep Face Deblurring." pp. 2015-2024, 10.1109/CVPRW.2017.252, 2017.

[2] JJM. Buiting, M. Bacon,"Using geophysical, geological, and petrophysical data to characterize reservoirs in the North Sea." in 5th Conference on Petroleum Geology of NW Europe, London. CD-ROM.

[3] X. Xiaoyu, L. Yun, S. Desheng, G. Xiangyu, and W. Huifeng, "Studying the effect of expanding low or high frequency on post-stack seismic inversion," in SEG Technical Program Expanded Abstracts 2012, pp. 1-5, September 2012.

[4] O. Russakovsky, J. Deng, H. Su, J. Krause, S. Satheesh, S. Ma, Z. Huang, A. Karpathy, A. Khosla, M. Bernstein, "Imagenet large scale visual recognition challenge," in ternational Journal of Computer Vision (IJCV), pp. 211252, 2015.

[5] N. Buduma, " Fundamentals of Deep Learning," Academic Press, in O'Reilly Media, 2015.

[6] R. Girshick, "Fast r-cnn," In IEEE Proceedings of International Conference on Computer Vision (ICCV), pp. 14401448, 2015.

[7] S. Bell, C. L. Zitnick, K. Bala, and R. Girshick, "Inside-outside net: Detecting objects in context with skip pooling and recurrent neural networks," in arXiv preprint arXiv:1512.04143, 2015.

[8] H. Nam and B. Han, "Learning multi-domain convolutional neural networks for visual tracking," In IEEE Proceedings of International Conference on Computer Vision and Pattern Recognition (CVPR) IEEE, 2016.

[9] K. He, X. Zhang, S. Ren, and J. Sun, "Deep residual learning for image recognition," In IEEE Proceedings of International Conference on Computer Vision and Pattern Recognition (CVPR). IEEE, 2016.

[10] A. Krizhevsky, I. Sutskever, G. E. Hinton, "Imagenet classification with deep convolutional neural networks: Advances in neural information processing systems," 2012, pp. 10971105.

[11] O. Abdel-Hamid, A.-r. Mohamed, H. Jiang, L. Deng, G. Penn, and D. Yu, "Convolutional neural networks for speech recognition," in IEEE/ACM Transactions on audio, speech, and language processing, num. 22, pp. 15331545, 2014.

[12] S. S. Farfade, M. J. Saberian, and L.-J. Li, 2015, "Multi-view face detection using deep convolutional neural networks," in Proceedings of the 5th ACM on International Conference on Multimedia Retrieval, ACM, pp. 643650.

[13] S. Ji,W. Xu, M. Yang, K. Yu, 2013, "3d convolutional neural networks for human action recognition," in IEEE transactions on pattern analysis and machine intelligence, num. 35, p. 221231.

[14] Q. Feng, Y. Miao, S. Ming-Jun, W. Yaojun, H. Guangmin, "Seismic facies recognition based on prestack data using deep convolutional autoencoder,".

[15] L. Lihui, L. Rong, L. Jianhai, Y. Wenkui, "Seismic Lithofacies Computation Method Based on Deep Learning," in International Geophysical Conference, pp. 649-652, April 2017.

[16] R. B. Latimer, R. Davidson, P. van Riel, "An interpreter's guide to understanding and working with seismic-derived acoustic impedance data," in The Leading Edge, pp. 242-256, vol. 19, num. 3, 2017.

[17] A. Buland, and H. Omre, "Bayesian linearized avo inversion," In Geophysics, 2003, pp. 185198.

[18] L. P. Figueiredo, M. Santos, M. Roisenberg, G. Neto, and W. Figueiredo, "Bayesian framework to wavelet estimation and linearized acoustic inversion," in Geoscience and Remote Sensing Letters, pp. 15, 2012.

[19] C. Wang, L. Sun, Z. Chen, S. Yang and J. Zhang, "High-quality non-blind motion deblurring," 2009 16th IEEE International Conference on Image Processing (ICIP), Cairo, 2009, pp. 153-156.

[20] H. Zhang, D. Wipf and Y. Zhang, "Multi-image Blind Deblurring Using a Coupled Adaptive Sparse Prior," 2013 IEEE Conference on Computer Vision and Pattern Recognition, Portland, OR, 2013, pp. 1051-1058.

[21] T.E. Bishop, S.D. Babacan, Amizic, T. Chan, R. Molina, and A. Katsaggelos, "Blind image deconvolution: problem formulation and existing approaches." in. Blindimage deconvolution: theory and applications, CRC press, 2007.

[22] S. D. Babacan, R. Molina, M. N. Do, and A. K. Katsaggelos, "Bayesian blind deconvolution with general sparse image priors." in Proceedings of European Conference on Computer Vision (ECCV), pp. 341355, 2012.

[23] D. Krishnan, T. Tay, and R. Fergus, "Blind deconvolution using anormalized sparsity measure." In CVPR, 2011.

[24] A. Levin, Y. Weiss, F. Durand, and W. T. Freeman. "Efficient marginal likelihood optimization in blind deconvolution." In CVPR, 2011.

[25] H. Zhang, J. Yang, Y. Zhang, N. M. Nasrabadi, and T. S. Huang, "Close the loop: Joint blind image restoration and recognition with sparse representation prior." in ICCV, 2011.

[26] F. Sroubek and P. Milanfar, "Robust multichannel blind deconvolution via fast alternating minimization." in IEEE Trans. on Image Processing, pp. 16871700, 2012.

[27] X. Zhu, F. Sroubek, P. Milanfar, "Deconvolving PSFs for a better motion deblurring using multiple images." in ECCV, 2012.

[28] A. Levin, Y. Weiss, F. Durand, and W. T. Freeman. "Understanding and evaluating blind deconvolution algorithms." In IEEE Proceedings of International Conference on Computer Vision and Pattern Recognition (CVPR), pp. 19641971.

[29] Y. Hacohen, E. Shechtman, and D. Lischinski, "Deblurring by example using dense correspondence." In IEEE Proceedings of International Conference on Computer Vision (ICCV), pp. 23842391, 2013.

[30] J. Pan, Z. Hu, Z. Su, and M. H. Yang, "Deblurring face images with exemplars." In Proceedings of European Conference on Computer Vision (ECCV), pp. 4762. Springer, 2014.

[31] W.S. Lai, J. B. Huang, Z. Hu, N. Ahuja, and M. H. Yang, "A comparative study for single image blind deblurring." In IEEE Proceedings of International Conference on Computer Vision and Pattern Recognition (CVPR). IEEE, 2016.

[32] A. Chakrabarti, "A neural approach to blind motion deblurring." In Proceedings of European Conference on Computer Vision (ECCV), pp. 221235. Springer, 2016.

[33] M. Hradis, J. Kotera, P. Zemck, and F. Sroubek, "Convolutional neural networks for direct text deblurring." In Proceedings of British Machine Vision Conference (BMVC), 2015.

[34] J. Sun, W. Cao, Z. Xu, and J. Ponce, "Learning a convolutional neural network for non-uniform motion blur removal." In IEEE Proceedings of International Conference on Computer Vision and Pattern Recognition (CVPR), pp. 769777, 2015.

[35] S. S. Sancevero, A. Z. Remacre, R. S. Portugal, "O papel da inverso para a impedncia no processo de caracterizao ssmica de reservatrios." in Revista Brasileira de Geofsica, p. 495-512, v. 24, 2006.

[36] P. J. Harvey, and D. J. MacDONALD, "Seismic modelling of porosity within the jurassic aged carbonate bank, offshore Nova Scotia," in Canadian Journal of Exploration Geophysics, num. 26, pp. 5471.

[37] G. Mavko, T. Mukerji, and J. Dvorkin, "The Rock Physics Handbook: Tools for Seismic Analysis of Porous Media." Cambridge: Cambridge University Press, pp. 359-369, 2009.

[38] H. DEBEYE, and P. RIEL van, "Lp-norm deconvolution." 1990, Geophysical Prospecting, pp. 381403

[39] S. Chopra, "Integrating coherence cube imaging and seismic inversion." The Leading Edge, pp. 354362, 2001.

[40] R. Dahl, M. Norouzi, and J. Shlens, "Pixel recursive super resolution" CoRR, 2017.

[41] V. Nair, and G. E. Hinton. "Rectified linear units improve restricted boltzmann machines." In Proc. 27th International Conference on Machine Learning, 2010.

[42] N. Qian, "On the momentum term in gradient descent learning algorithms," in Neural Networks, vol. 12, pp. 145-151, 1999.

[43] S. Narayana, and P. K. Thirivikraman, "Image similarity using fourier transform," in International Journal of Computer Engeneering and Technology, 2015, num. 6, pp. 2937.
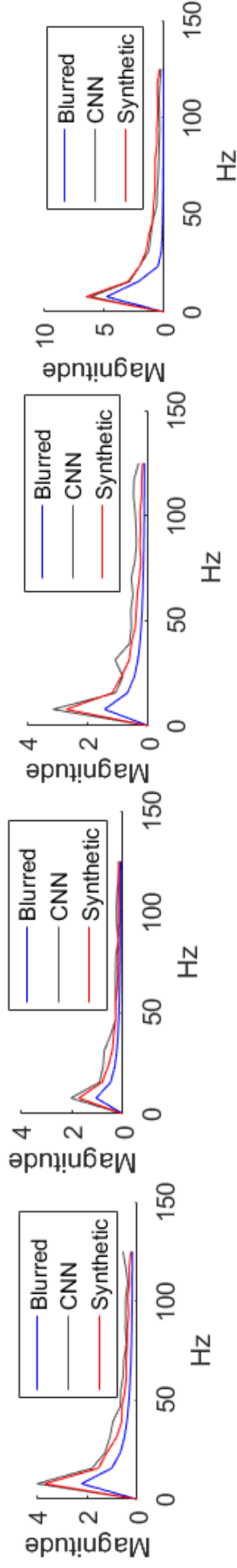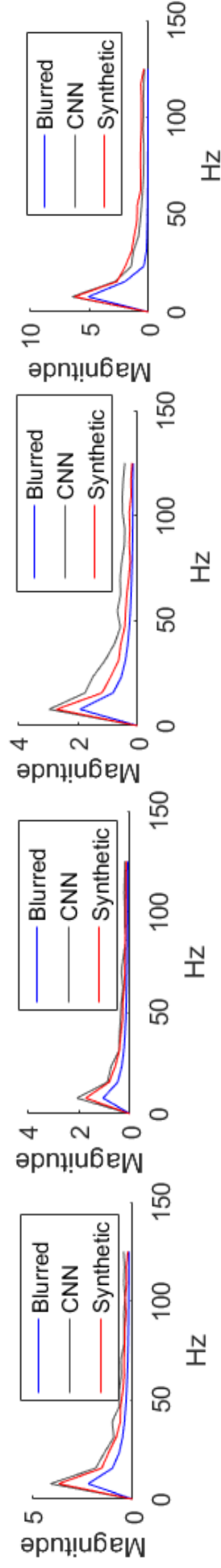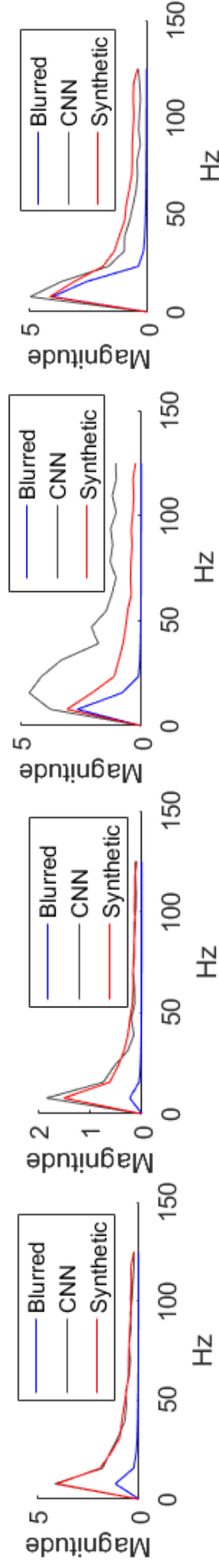
(a) First test case.
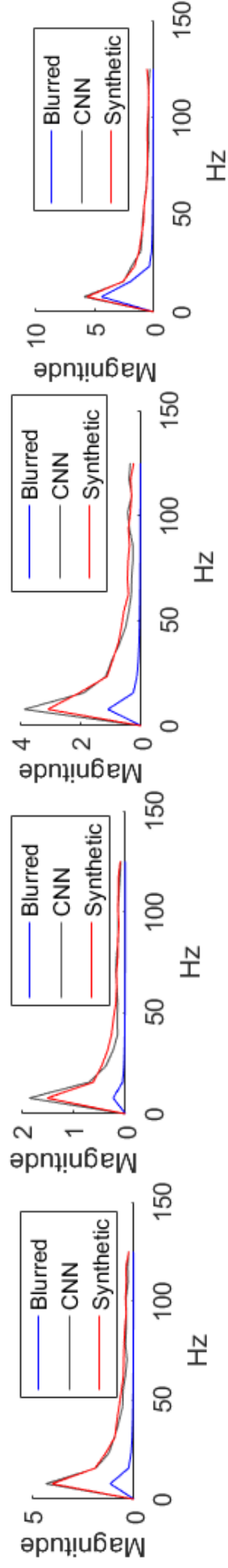
(b) Second test case.

(c) Third test case.

(d) Fourth test case